

Active Assembly of Spheroidal Photocatalytic BiVO<sub>4</sub> Microswimmers

Sandra Heckel, Jens Grauer, Maria Semmler, Thomas Gemming, Hartmut Löwen, Benno Liebchen, and Juliane Simmchen\*

Cite This: *Langmuir* 2020, 36, 12473–12480

Read Online

ACCESS |



Metrics &amp; More

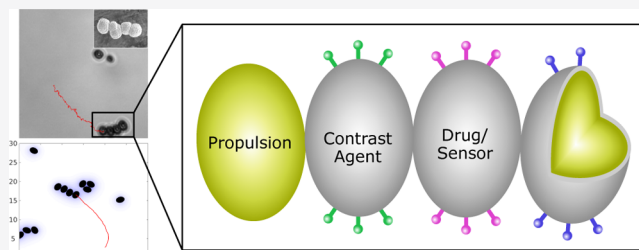


Article Recommendations



Supporting Information

**ABSTRACT:** We create single-component photocatalytic bismuth vanadate (BiVO<sub>4</sub>) microswimmers with a spheroidal shape that move individually upon irradiation without any asymmetrization step. These particles form active assemblies which we investigate combining an experimental approach with numerical simulations and analytical calculations. We systematically explore the speed and assembly of the swimmers into clusters of up to four particles and find excellent agreement between experiment and theory, which helps us to understand motion patterns and speed trends. Moreover, different batches of particles can be functionalized separately, making them ideal candidates to fulfill a multitude of tasks, such as sensing or environmental remediation. To exemplify this, we coat our swimmers with silica (SiO<sub>2</sub>) and selectively couple some of their modules to fluorophores in a way which does not inhibit self-propulsion. The present work establishes spheroidal BiVO<sub>4</sub> microswimmers as a versatile platform to design multifunctional microswimmers.



## INTRODUCTION

Numerous applications have been proposed for catalytic microswimmers in the recent past. Researchers are currently probing their potential for sensing,<sup>1</sup> drug delivery,<sup>2</sup> and environmental remediation.<sup>3</sup> To create an asymmetry in fuel degradation which is essential for swimming, hemispherical metal coating is the method of choice in most examples.<sup>4</sup> Even though it is not limited to spheres,<sup>5</sup> this process requires perfect monolayers of particles and therefore limits the throughput of microswimmer production. Moreover, it excludes half of the swimmer surface from additional functionalization. Mostly, potential applications then depend on further modification with sensing/contrast agents or a drug to add functionality. This makes complicated and costly multistep fabrication not suitable for upscaling, which is highly desired because collective interactions are often a prerequisite to successfully fulfill a task.

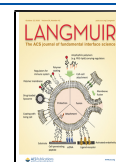
As an alternative approach to create self-propulsion, researchers have recently developed a modular concept to microswimming, opening up the possibility of reconfigurable swimmers that can fulfill multiple tasks because of differently modified building blocks. One advantage of this approach is that different and possibly competing functionalities of the swimmers no longer have to be implemented in a single particle but can be distributed among their modules. Thus, the number of fabrication steps on one swimmer particle as well as the risk of reactions impeding each other decreases. To overcome these limitations, some material-specific binary assemblies have already been proposed in the past,<sup>6,7</sup> but mostly, laborious synthetic strategies are required.<sup>8</sup>

Modular microswimmers can generally be divided into rigidly bound and dynamic structures, where dynamic structures bear the clear advantage of reconfigurability.<sup>9</sup> After several examples of the assembly observed in classical Janus particles<sup>10,11</sup> and droplets,<sup>12</sup> Niu et al. have constructed ion-exchange-driven modular microswimmers.<sup>13</sup> Here, passive cargo particles assemble around cationic exchange particles.<sup>14,15</sup> Kei Cheang et al. have assembled magnetic microspheres into modular swimmers in a Helmholtz coil setup,<sup>16</sup> and also, electric fields have been explored extensively.<sup>17,18</sup> Schmidt et al. in turn have combined absorbing (active) and nonabsorbing (passive) particles in a subcritical liquid mixture. Illumination with laser light then leads to a temperature increase around absorbing particles and therefore to attraction among different colloids. The so-formed “colloidal molecules” show directed motion caused by the response of the nonabsorbing particles to the temperature and concentration gradient surrounding the absorbing particles.<sup>19</sup> All of the mentioned examples consist of spherical particles, which only become active upon assembly. More examples have recently been described theoretically<sup>20,21</sup> and discussed in reviews.<sup>9,22</sup> A different approach was followed by the Tierno group, who relied on dominating magnetic interactions.<sup>23,24</sup>

Received: May 27, 2020

Revised: August 21, 2020

Published: August 21, 2020



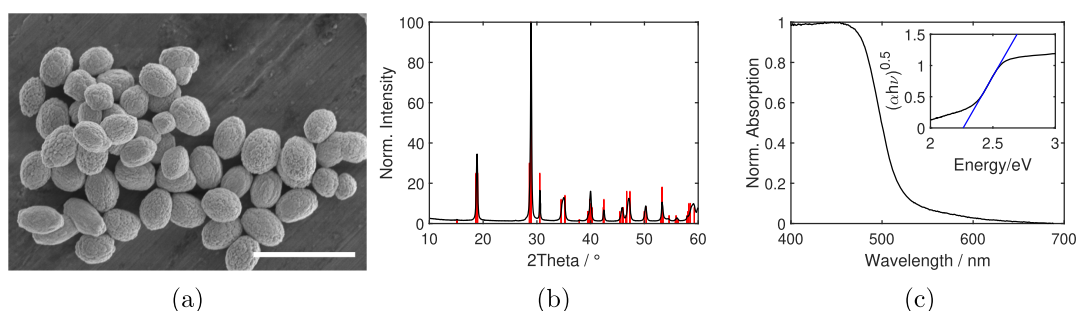


**Figure 1.** Material properties of  $\text{BiVO}_4$  microparticles. (a) SEM image. The spheroidal particles have an average length of  $2.09 \mu\text{m}$  and an average width of  $1.54 \mu\text{m}$ , which results in an aspect ratio of 1.37. The scale bar is  $5 \mu\text{m}$ . (b) XRD pattern of the particles (black) agrees with the monoclinic scheelite crystal structure (red) (JCPD 14-688) of  $\text{BiVO}_4$ . (c) Normalized DRS spectrum and Tauc plot show an indirect band gap of 2.26 eV.

In this work, we present microswimmers based on spheroidal bismuth vanadate building blocks, which self-propel and self-organize into a variety of active assemblies of different geometries and speeds. We call them modular swimmers, although in contrast to the aforementioned examples, single particles (modules) also show activity and an assembly is not required for active motion. As a particularly interesting property,  $\text{BiVO}_4$  swimmers, which we<sup>25</sup> and others<sup>26</sup> have recently introduced, can self-propel without any asymmetrization of their surface. Instead, these photocatalytic swimmers show an internal asymmetric distribution of electrons and holes upon excitation which results in a net propulsion. This further reduces the number of required preparation steps, and, accordingly, active swimmers can be obtained without the throughput-limiting process of hemispherical metal deposition. In the present work using a combined approach based on experiments and numerical simulations, we systematically explore the interactions between single swimmers and how the resulting aggregates move depending on their conformation. We modified the particles with a silica shell, which enables easy functionalization with a variety of entities, such as fluorophores or positively charged amino groups, and demonstrate combined swimmers of pristine and functionalized  $\text{BiVO}_4$  modules.

## RESULTS AND DISCUSSION

**Characterization of Single  $\text{BiVO}_4$  Swimmers.**  $\text{BiVO}_4$  microparticles were synthesized via a solvothermal approach. Figure 1a shows the obtained spheroidal particles, with an average length of  $2.09 \pm 0.22 \mu\text{m}$ , a width of  $1.54 \pm 0.15 \mu\text{m}$ , and an aspect ratio of  $1.37 \pm 0.13$ . A histogram with particle size distribution can be found in Figure S1a. A closer look on the particles reveals a rough, highly structured surface, indicating their formation from smaller nano- and microsized crystals during the synthesis process (see also Figure S1b). As  $\text{BiVO}_4$  is an oxidic material, the surface charge in neutral pH regimes is generally negative for this material. This is proven by a negative zeta potential of  $-26.3 \text{ mV}$ .

Naturally,  $\text{BiVO}_4$  appears in three different crystal structures, of which monoclinic scheelite is the photocatalytically most active one.<sup>27</sup> As can be seen in Figure 1b, the particles synthesized here are in good agreement with the powder X-ray diffraction (XRD) pattern of monoclinic scheelite, which is an important prerequisite for photochemical microswimmers. Additionally, the absorption spectrum derived by diffuse reflectance spectroscopy (DRS) in Figure 1c proves absorption up into the visible range for these particles with a band gap of

2.26 eV, implying that propulsion with ultraviolet (UV) as well as blue light can be achieved. To prove this, we determined the speed of single particles under UV and blue excitation. However, for the following experiments with active assemblies and functionalized particles, only UV excitation was applied.

**Locomotion Mechanism.** To induce directed motion, it is sufficient to immerse these particles in a 0.3% hydrogen peroxide ( $\text{H}_2\text{O}_2$ ) aqueous solution and excite them with 385 nm UV or 469 nm blue light. Figure 2a shows the reaction

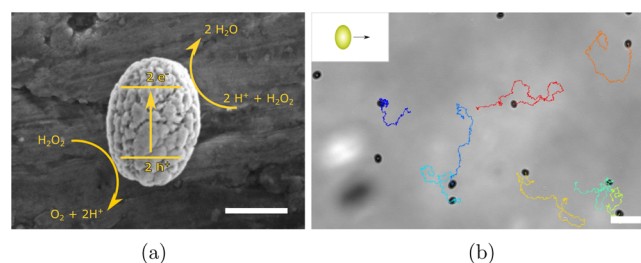


**Figure 2.** Motion mechanism and pattern of single particles. (a) Mechanism of  $\text{H}_2\text{O}_2$  fuel degradation, integrated in a SEM image. The choice of reduction and oxidation spots in this image is for illustrative purposes only and does not necessarily represent the actual reaction distribution. The scale bar is  $1 \mu\text{m}$ . (b) Tracks of single pristine  $\text{BiVO}_4$  swimmers under UV illumination for 30 s. The scale bar is  $5 \mu\text{m}$ .

mechanism of  $\text{H}_2\text{O}_2$  fuel degradation. Upon excitation,  $\text{H}_2\text{O}_2$  reacts with holes in the crystal to produce oxygen and hydrogen ions. These cations are consumed by the other half-reaction, where  $\text{H}_2\text{O}_2$  reacts with electrons in the crystal to water. A proton gradient is thus created around the particle that induces directed motion, which, if compared to pure Brownian motion, can be distinguished by the faster growth of its mean-square displacement (MSD) (see Figure S2). It should be highlighted that these particles do not require any additional asymmetrization to perform active motion but can directly be used as single-component swimmers. The reason for this unique behavior can be twofold: the monoclinic scheelite crystal structure favors electron–hole separation onto different facets,<sup>28,29</sup> thus spatially separating the oxidation and reduction half-reactions of  $\text{H}_2\text{O}_2$  degradation when excited with light. Therefore, an intrinsic driving force for a fuel gradient around the particle is provided.<sup>30</sup> Figure 2b shows trajectories of single spheroidal swimmers at low concentration and emphasizes that the particles move mainly perpendicular to their long axis (see also Videos S1 and S2). This strengthens

the assumption that the crystal has a certain orientation within these particles so that the oxidation and reduction sites are intrinsically separated. We additionally assume the effect to be enhanced by the nano- and microstructured appearance of the particle surface as irregularities on the surface can enhance the development of a fuel gradient around the particle.

In general, it is also possible to consider environmental fluctuations or the vicinity of other particles as a potential drive for directed motion. However, in our previous work about square-shaped BiVO<sub>4</sub> microswimmers, we excluded these because of the rather large size that minimizes the influence of random fluctuations and observed particle swimming behavior upon repeated excitation cycles.<sup>25</sup> Here, we have shown that the particles always move in the same direction in consecutive excitation cycles, independent of their surroundings. Similar particle dimensions and behavior in this work suggest again a dominant importance of the catalytic properties.

The speed of these single spheroidal swimmers spreads between 3 and 6  $\mu\text{m s}^{-1}$ , with an average of  $4.20 \pm 0.71 \mu\text{m s}^{-1}$  for UV light and  $4.47 \pm 0.57 \mu\text{m s}^{-1}$  for blue light (the values are also summarized in Table 1).

**Table 1. Mean Speeds and Standard Deviations for Different Modular Conformations, Retrieved from Experiments (under UV Excitation) and Simulations<sup>a</sup>**

number of modules	mean speed/ $\mu\text{m s}^{-1}$ (experiment)	mean speed/ $\mu\text{m s}^{-1}$ (simulation)	percentage of swimmers/%
1	$4.20 \pm 0.71$	$4.23 \pm 0.59$	46
2	$3.83 \pm 0.73$	$3.92 \pm 0.63$	23
3-caterpillar	$3.70 \pm 0.49$	$3.76 \pm 0.85$	7
3-triangle	$3.32 \pm 0.21$	$3.07 \pm 0.59$	9
others			15

<sup>a</sup>We observe a trend for a decreased speed with an increasing amount of particles in one swimmer. Also, the percentage of swimmers after 15 s was obtained from simulations. The simulation parameters are as in Figure 3.

**Active Assemblies.** If the swimmers are at higher concentration so that random particle–particle encounters are more likely, we observe that they attract each other over a distance of more than two particle radii, leading to self-propelled assemblies. While these attractions can originate from different effects, as discussed previously by Wang et al.,<sup>3</sup> photochemical swimmers such as ours are mostly subject to hydrodynamic and chemical-field-induced interactions. As shown in Figure 2, the overall product of the reaction is oxygen, while the produced protons are directly consumed in the oxidation reaction. We speculate that this interplay contributes to favorable attraction between individual modules. Additionally, the hydrodynamic flows created by the oxygen gradient as well as the migrating protons also seem to favorably influence the attraction.

We observe recurring geometries of swimmers consisting of up to four modules, which can be seen in Figure 3 (see also Video S3). In contrast to the work of Perry et al.,<sup>31</sup> these active assemblies do not reconfigure or fluctuate between different geometries but rather keep on growing over time. The longer the swimmers are illuminated with UV light, the larger the modular swimmers get, leading to actively moving agglomerates of many more than four modules. The motility then

decreases strongly, and these active clusters require a separate consideration which is beyond the scope of this article.

In general, it can be noted that contingent on their spheroidal shape, the particles mainly attract each other perpendicularly to their long axis. Although these are single-component swimmers, their shape introduces favorable modular conformations without the need to induce them externally. This represents a strong difference from previous works where individual modules usually consist of isotropic, spherical particles.<sup>14,16,19</sup>

Examples for experimental swimmer trajectories with reproducible geometries of two, three, and four modules are displayed in Figure 3a. In the simulation model, these swimmers produce a chemical field to which they respond themselves. This results in self-propulsion as well as in an attraction of other swimmers. The resulting assemblies then show the same geometries as those in the experiment and move on similar trajectories (Figure 3b). More experimental and simulated trajectories can be found in Figure S3.

For swimmers consisting of two modules, only one stable conformation exists. If three modules are combined into a swimmer, two different stable conformations are found. First, we observe a “caterpillar” structure, where all three spheroids are lined up along their short axis. Second, a “triangle” assembly is observed, with the third module not being aligned along the short axis but interacting with the short ends of the other two modules. This leads to a more compact structure. Finally, two different conformations with four modules are observed as well. Analogous to the three modular swimmers, a caterpillar is formed. A more compact assembly is called the “rectangle” conformation. It should be noted that especially the caterpillar structures can only be formed because of the spheroidal shape of the particles and have only been possible to be achieved through magnetic interactions earlier.<sup>24</sup>

Once the particles assemble into modular swimmers, their motion patterns change compared to those of single swimmers. As can be seen in all trajectories in Figure 3, we observe a tendency for curved trajectories of modular swimmer conformations in both the experiment and simulation. Moreover, for swimmers consisting of three and four modules, the trajectory radii of the more compact conformations (triangle and rectangle) appear to be smaller as compared to those of elongated caterpillar conformations. An explanation for this can be found in the forces affecting the swimmer, which result from the gradient field around it. In addition to a longitudinal propulsion force, a triangular swimmer also experiences a torque, which results in a more curved trajectory, as will be discussed in more detail in the framework of our theoretical model below (see also Figure S4).

Let us now systematically examine how often the different modular swimmers occur in our simulations, that is, we assess the frequency at which certain conformations appear and evaluate their occurrence after 15 s. The results can be found in Table 1. As expected, single particles are observed most frequently, followed by assemblies consisting of two and then three modules. Swimmers consisting of four modules appear too rarely to give statistically validated information on the speed or the ratio between the caterpillar and rectangle swimmers. As a general trend, we find that larger swimmers move slower. This is observed in experiments as well as in simulations, which are in excellent qualitative agreement (see Figure 4). An explanation can be found in the overall concentration gradient surrounding a cluster, which is less

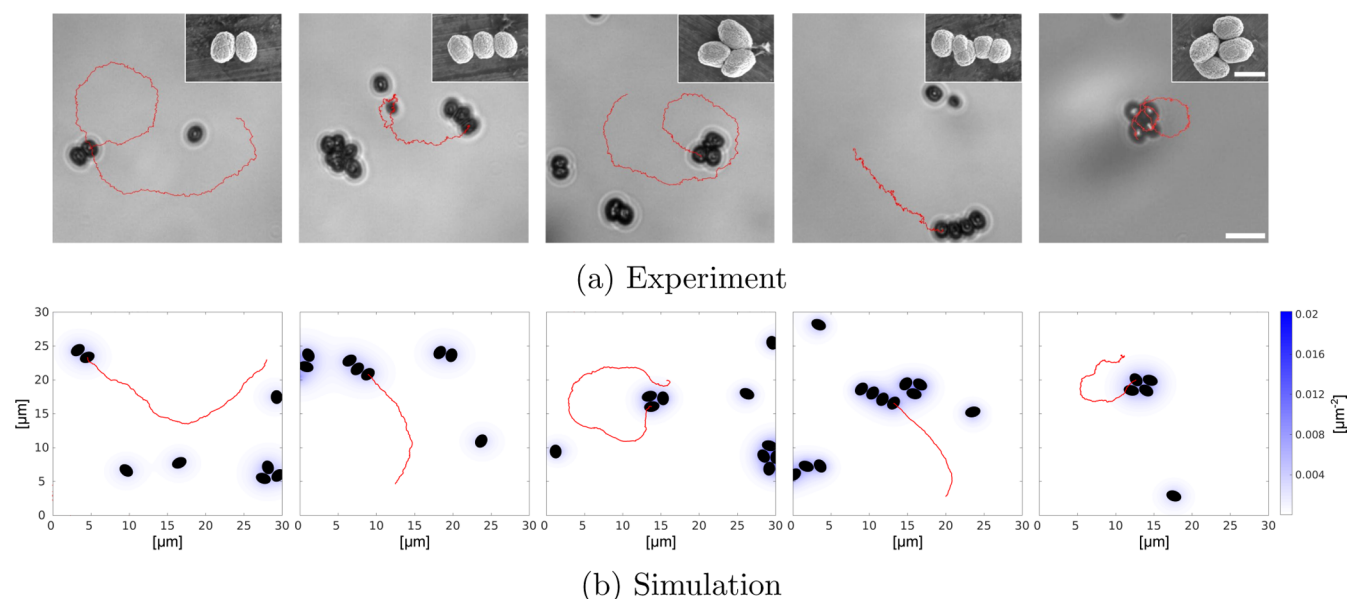


**Figure 3.** Exemplary tracks of modular swimmers after 20 s consisting of two to four particles in experiments and simulations. (a) Experimental tracks of two, three-caterpillar, three-triangle, four-caterpillar, and four-rectangle particle assembly. The scale bar is 5  $\mu\text{m}$ . Insets represent SEM images of exemplary assembled particles with the corresponding structure. The inset scale bar is 2  $\mu\text{m}$ . (b) Simulated tracks. The shown box length is  $L = 30 \mu\text{m}$ , and the color shows the concentration of the solute. Simulation parameters:  $N = 60$ ,  $L_{\text{box}} = 100 \mu\text{m}$ ,  $k_0 = 70 \text{ s}^{-1}$ ,  $k_d = 0.7 \times 10^3 \text{ s}^{-1}$ ,  $\alpha/\gamma = \alpha_r/\gamma = 80 \times 10^3 \mu\text{m}^4 \text{ s}^{-1}$ ,  $D_c = 1.4 \times 10^3 \mu\text{m}^2 \text{ s}^{-1}$ ,  $D = 0.1 \mu\text{m}^2 \text{ s}^{-1}$ ,  $D_r = 0.1 \text{ s}^{-1}$ , and  $\epsilon/\gamma = 100 \mu\text{m}^2 \text{ s}^{-1}$ .

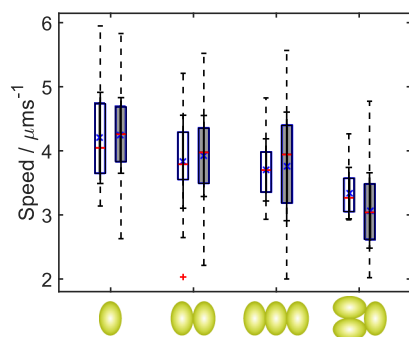


**Figure 4.** Mean speeds of swimmers consisting of one, two, and three particles under UV excitation. White boxes represent experimental data, whereas gray boxes show simulated data. Boxes indicate the interquartile range, the red line is the respective median, and dotted lines show the maximum and minimum values. For comparison, the mean values are marked with a blue cross (“ $\times$ ”) and the standard deviation is displayed in solid black lines. The red cross represents an outlier data point. The simulation parameters are as in Figure 3.

pronounced for larger clusters. In the caterpillar configuration, for example, the chemical field produced by the central colloid attracts both of its neighbors and therefore hardly contributes to the motion of the cluster. However, it still provides drag and therefore effectively slows down the assembled swimmer. Note that in our simulations, we have chosen the same particle density as in our experiments. When choosing a higher particle density instead, larger aggregations form faster and are therefore more frequently present at a given time than for a low density. At late times, the clusters merge and form larger and larger clusters, finally resulting in one macrocluster containing most of the particles in our simulations.

**Functionalized Particles and Active Assemblies.** A strong advantage of modular microswimmers in terms of possible applications is the absence of the need to fit all desired functionalities into one single particle. Here, we demonstrate a

very versatile functionalization approach for our  $\text{BiVO}_4$  swimmers. By coating the as-synthesized particles with a thin shell of silicon dioxide ( $\text{SiO}_2$ ), we introduce a coupling possibility to a variety of different entities. Because of facile and universal coupling protocols, nontoxic  $\text{SiO}_2$  has been used for decades as a carrier material, for example, fluorophores,<sup>32</sup> drugs,<sup>33</sup> and enzymes.<sup>34</sup> Figure 5a shows an exemplary

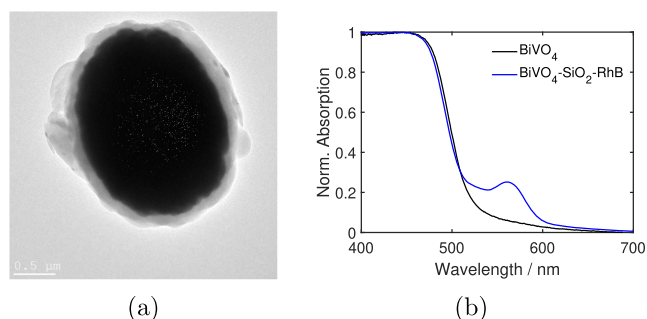


**Figure 5.** Material properties of  $\text{SiO}_2$ -coated particles. (a) TEM image of a  $\text{SiO}_2$  shell-coated  $\text{BiVO}_4$  particle. (b) DRS spectra of pristine and RhB-functionalized swimmers. The band gap remains unaffected by the functionalization, and the absorption peak of the dye appears.

transmission electron microscopy (TEM) image of a successfully coated  $\text{BiVO}_4$  particle. Scanning TEM in combination with energy-dispersive X-ray spectroscopy (STEM-EDX) confirms the  $\text{SiO}_2$  identity of the shell (see Figure S5), which is around 150 nm thick.

We now modify the silica shell with different functional groups to demonstrate the functionality of this process. First, we bind the fluorescent dye rhodamine B (RhB) to distinguish shelled and pristine swimmers by fluorescence. Figure 5b confirms the successful coupling to the dye by an additional peak appearing in the DRS spectrum, which can be identified as the absorption peak of RhB. The speed of these

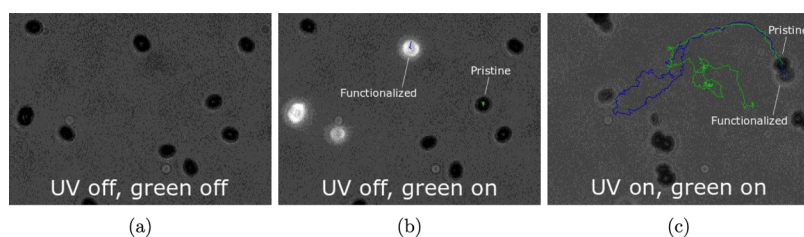


**Figure 6.** Microscope snapshots of mixed pristine and RhB-functionalized particles. (a) Particles without green or UV illumination. (b) Particles under green illumination. The functionalized particles absorb the light and can be detected via fluorescence of the dye. (c) Particles under green and UV illumination after 45 s. A combined swimmer consisting of a pristine (green trajectory) and a functionalized (blue trajectory) module has formed. For better recognizability, the concerned fluorescent particle has been marked in (b,c). As the dye bleaches over time, detection becomes more challenging.

functionalized swimmers remains almost unchanged compared to that of single pristine swimmers at  $4.19 \pm 0.48 \mu\text{m s}^{-1}$ , suggesting a certain porosity of the  $\text{SiO}_2$  shell. Also, the surface charge of these swimmers remains negative (zeta potential:  $-22.4 \text{ mV}$ ) as  $\text{SiO}_2$  commonly has a negative zeta potential at neutral pH values. Figure 6 shows a mixture of functionalized and pristine swimmers under the microscope. Whereas in Figure 6a, all particles optically appear to be the same, illumination with green light (555 nm) excites RhB and reveals three fluorescent particles in Figure 6b. If additionally UV light is turned on, the particles start to move actively and form assemblies consisting of fluorescent and pristine units, as can be seen in Figure 6c. See also Video S4 for more examples of mixed assemblies.

Second, we also modified our silica shell with (3-aminopropyl)triethoxysilane (APTES) to invert the surface charge to positive, caused by positively charged amino groups which lead to a zeta potential of  $+41.0 \text{ mV}$  at neutral pH. By this, we overcome the limitation to negatively charged substrates as swimmer environments and broaden the possible field of application to more complex environments. We demonstrate successful active motion on positively charged surfaces (see Figure S6), which would otherwise lead to attractive forces between particles and the surface and therefore inhibit active motion.

The formation of combined assemblies with and without functionality demonstrated here opens up numerous functionalization opportunities for photochemical microswimmers, without concerns about numerous fabrication steps that inhibit upscaling. We envision that these results pave the way for the development and application of multifunctional modular swimmers and their theoretical understanding.

## CONCLUSIONS

To summarize, in this article, we develop modular microswimmers made from  $\text{BiVO}_4$  that are able to undergo self-propelled motion without any asymmetrization step in the manufacturing process, overcoming the throughput limits of hemispherical metal coating and enabling large-scale microswimmer synthesis. After irradiation with UV light, individual modules start moving and eventually meet their peers to form assemblies. We explore their motion experimentally as well as in numerical simulations, finding excellent agreement between both. We furthermore apply analytical calculations to understand speed distributions as well as motion patterns of these active assemblies. The present work broadens the variety of active components available for modular microswimming, adding the options of photocatalytic propulsion as well as new shapes.

In a second part, we demonstrate that the developed modular microswimmers serve as a useful platform for implementing functionalities. In particular, we show that neither the motility nor the formation of assemblies is inhibited by covering the individual spheroids by a thin silica layer. This coverage allows multiple functionalizations to increase the range of capabilities beyond simple self-propulsion. To exemplify this, we add a fluorescent dye to improve detection and facilitate discrimination between the pristine and functionalized modules. We also demonstrate an inversion of the surface charge from negative to positive by functionalizing the silica shell with APTES. This enables the swimmers to move on positively charged surfaces. In the future, it would be interesting to explore the large-scale collective behavior of  $\text{BiVO}_4$  microswimmers, possibly leading to dynamic clustering,<sup>35</sup> and to examine  $\text{BiVO}_4$  microswimmers with magnetic interactions. Different batches of modules can then be functionalized with different agents, paving the way for combining different tasks such as guidance, drug transport, sensing, or imaging in the final assembly.

## EXPERIMENTAL SECTION

**Synthesis of Bismuth Vanadate Microparticles.** The synthesis is based on a protocol reported previously by Jiang et al. with some modifications.<sup>36</sup> Briefly, 2.5 mL of concentrated nitric acid and 2.78 g (15 mmol) of dodecylamine were added to 12.5 mL of a 1:1 ethanol/ethylene glycol mixture under stirring. Then, 2.425 g (5 mmol) of bismuth nitrate pentahydrate and 0.585 g (5 mmol) of ammonium metavanadate were added and dissolved. With 2 M NaOH in a 1:1 ethanol/ethylene glycol mixture, the pH was adjusted to 2. Next, the solution was transferred to a Teflon-lined stainless steel autoclave and left to ripen for 3 h. Subsequently, it was treated hydrothermally at  $100 \text{ }^\circ\text{C}$  for 12 h. After centrifugation and repeated washing with ethanol and water, the sample was dried at  $60 \text{ }^\circ\text{C}$  for 12 h and stored under air.

**Silica Coating of Microparticles and Functionalization.** To increase surface reactivity, 100 mg of bismuth vanadate microparticles was dispersed in 10 mL of 1 M nitric acid and sonicated for 15 min. After centrifugation, the supernatant was discarded and particles were redispersed in 10 mL of 0.01 M citric acid. After sonication for 15 min and centrifugation, 4 mL of deionized water and 4  $\mu\text{L}$  of concentrated ammonia were added to the particles. In a glass vial, a mixture of 15 mL of ethanol, 4.7 mL of deionized water, and 0.3 mL of concentrated ammonia were prepared. After adding the particle dispersion to this vial, 100  $\mu\text{L}$  of tetraethyl orthosilicate (TEOS) was added under vigorous stirring. After 20 min, another 100  $\mu\text{L}$  of TEOS was added. After being stirred at room temperature overnight, the dispersion was centrifuged and washed with ethanol and deionized water before storing the sample in 1 mL of deionized water.

For functionalizing with rhodamine, 10 mg of RhB isothiocyanate was dissolved in 10 mL of dimethyl sulfoxide. After adding 8.6  $\mu\text{L}$  of APTES under stirring, the solution labeled as RITC-APTES was

stirred overnight at room temperature and stored in the dark afterward. In a glass vial, 0.3 mL of the silica-coated bismuth vanadate particles was dispersed in 15 mL of isopropanol. After addition of 1.5 mL of concentrated ammonia, 100  $\mu\text{L}$  of TEOS was added dropwise, followed by 150  $\mu\text{L}$  of RITC-APTES. After being stirred overnight in the dark, particles were washed with ethanol and water extensively. To remove excess silica, the sample was centrifuged at 1000 rpm repeatedly and the supernatant was discarded. The particles were dispersed in deionized water and stored in the dark at 8  $^{\circ}\text{C}$ .

For functionalizing with APTES, 10 mg of  $\text{SiO}_2$ -shelled  $\text{BiVO}_4$  particles was dispersed in 10 mL of isopropanol. After addition of 1.5 mL of concentrated ammonia, particles were sonicated for 10 min. APTES (20  $\mu\text{L}$ ) was added under stirring at room temperature, and the solution was stirred overnight. After washing with ethanol and deionized water four times, the particles were dispersed in deionized water and stored under ambient conditions.

**Microscopy Experiments.** Experiments were conducted on an inverted Zeiss microscope with a Colibri 7 light source. Spheroidal  $\text{BiVO}_4$  particles of a few milligrams were dispersed in deionized water and sonicated for 3 min. Then, samples were prepared on a 24  $\times$  24 mm glass slide by mixing 6.5  $\mu\text{L}$  of deionized water with 3  $\mu\text{L}$  of 1%  $\text{H}_2\text{O}_2$  and 0.5  $\mu\text{L}$  of  $\text{BiVO}_4$  dispersion.

For experiments with functionalized/nonfunctionalized particle mixtures, 6  $\mu\text{L}$  of deionized water, 3  $\mu\text{L}$  of 1%  $\text{H}_2\text{O}_2$ , and 0.5  $\mu\text{L}$  of the functionalized and nonfunctionalized particle solutions each were combined on a 24  $\times$  24 mm glass slide. Samples were illuminated with a green (555 nm, 50 mW) light-emitting diode (LED) for RhB excitation and a UV (385 nm, 315 mW) or blue (469 nm, 230 mW) LED for propulsion.

For experiments with positively charged swimmers, substrates (cover glasses) were modified with APTES through a gas-phase reaction to induce a positive charge. Deionized water (6  $\mu\text{L}$ ), 3  $\mu\text{L}$  of 1%  $\text{H}_2\text{O}_2$ , and 1  $\mu\text{L}$  of the particle solution were combined on the modified glass slide and illuminated with a UV LED for propulsion.

**Scanning Electron Microscopy.** For scanning electron microscopy (SEM) imaging, diluted solutions of  $\text{BiVO}_4$  microparticles were drop-cast on aluminum tape-coated sample holders and dried overnight. The images were obtained using a Zeiss DSM 982 GEMINI electron microscope.

**TEM.** For TEM imaging, diluted solutions of microparticles were drop-cast on carbon-coated copper TEM grids and dried under vacuum overnight. Images were taken on an FEI Tecnai F30 microscope (300 kV). The same device was used for STEM.

**Powder X-ray Crystallography.** XRD patterns were acquired using a Bruker 2D phaser in a  $2\theta$  range of 10–100 $^{\circ}$ , where symmetrical scans were performed. The microparticles were dispersed in ethanol and drop-cast on a Si wafer.

**DRS.** DRS measurements were recorded in diluted aqueous particle solutions using a Cary 60 spectrophotometer (Agilent Technologies).

**Video Evaluation.** Videos were tracked with the Fiji plugin TrackMate,<sup>37</sup> and the resulting trajectory files were processed with a MATLAB script and with the help of the msd analyzer function package.<sup>38</sup> For single particles as well as each assembly configuration, the averaged instantaneous speeds over at least 400 frames (10 s) were calculated for at least 20 independent trajectories from different sessions. The average of these speeds was calculated to determine the mean speed of a specific assembly conformation. The MSD curves were calculated with the msd analyzer function as well, and the weighted average of several curves was determined for the MSD.

**Model.** To model our experimental findings, we consider an ensemble of  $N$  overdamped spheroidal colloids at position  $\mathbf{r}_i$  and with orientation  $\hat{\mathbf{u}}_i$  in two spatial dimensions, where  $i$  is the particle index. The photochemical reaction on the particles causes an asymmetric internal distribution of electrons and holes, and hence, a chemical concentration field (or “solute”)  $c(\mathbf{r}, t)$  is asymmetrically produced (catalyzed) with a rate  $k_0$  (see Figure 7) to which all colloids in the system respond. Effectively, the production occurs predominantly along one of the long sides of the spheroids which causes both self-propulsion and cross-interactions among the particles such that no explicit self-propulsion term is required in our equations of motion

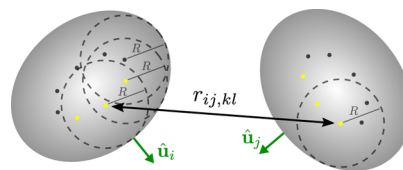


**Figure 7.** Schematic of the implementation of the model: two spheroidal colloids constructed by an arrangement of partly overlapping spheres with radius  $R$  and segment–segment distance  $r_{ij,kl}$ . The solute is produced on one long side of the colloids (yellow marked segments).

(similar to that in ref 39). To describe the dynamics of the particle motion, we use Langevin equations ( $i = 1, \dots, N$ ) coupled to the self-produced chemical field  $c(\mathbf{r}, t)$ <sup>40–43</sup>

$$\begin{aligned} \mathbf{f}_T \partial_t \mathbf{r}_i(t) &= \alpha \nabla_{\mathbf{r}_i} c - \nabla_{\mathbf{r}_i} V + \sqrt{2D} \mathbf{f}_T \boldsymbol{\eta}_i, \\ \mathbf{f}_R \partial_t \hat{\mathbf{u}}_i(t) &= \alpha_{\mathbf{r}_i} \nabla_{\hat{\mathbf{u}}_i} c - \nabla_{\hat{\mathbf{u}}_i} V + \sqrt{2D_{\mathbf{r}_i}} \mathbf{f}_R \boldsymbol{\xi}_i \end{aligned} \quad (1)$$

Here,  $D$  is the diffusion coefficient of the particles,  $D_{\mathbf{r}_i}$  is the effective rotational diffusion rate around the short axis of the particles,  $\boldsymbol{\eta}_i(t)$  and  $\boldsymbol{\xi}_i(t)$  represent unit-variance Gaussian white noise with zero mean, and  $\nabla_{\hat{\mathbf{u}}_i}$  is the gradient on the unit circle (see refs 44 and 45). The matrices  $\mathbf{f}_T$  and  $\mathbf{f}_R$  represent the translational and rotational friction tensors determined by the Perrin coefficients for a spheroid<sup>46</sup> and the Stokes friction coefficient  $\gamma$  of a sphere of an equivalent volume, respectively. The coupling coefficient of the particles to the solute is denoted as  $\alpha$ , where  $\alpha > 0$  leads to phoretic attraction and  $\alpha < 0$  results in phoretic repulsion among the colloids. In addition,  $V$  accounts for steric repulsions among the spheroids, represented by Weeks–Chandler–Anderson (WCA) repulsions here.

**Details on the Implementation.** For simplicity, we approximate each spheroidal colloid as a rigid body of  $m$  partly overlapping spheres, called “segments” in the following (see Figure 7). To describe the steric repulsions, we let all segment–segment pairs belonging to different particles interact through a repulsive WCA potential  $V = \frac{1}{2} \sum_{i,j \neq i} V_{ij}$ , where the sums run over all particles and where  $V_{ij} = \frac{4\epsilon}{m^2} \sum_{k=1}^m \sum_{l=1}^m \left[ \left( \frac{\sigma}{r_{ij,kl}} \right)^{12} - \left( \frac{\sigma}{r_{ij,kl}} \right)^6 \right] + \epsilon$  if  $r_{ij,kl} \leq 2^{1/6} \sigma$  and 0 otherwise. Here,  $\epsilon$  determines the strength of the potential,  $r_{ij,kl}$  denotes the Euclidean distance between segment  $k$  of particle  $i$  and segment  $l$  of particle  $j$ ,  $r_c = 2^{1/6} \sigma$  indicates a cutoff radius beyond which the potential energy is 0, and  $\sigma = 2R$  is the segment diameter.

The solute  $c(\mathbf{r}, t)$  is produced on one long side of the particles (yellow marked segments at position  $\mathbf{r}_{i,k}$  in Figure 7). The dynamics of  $c$  follows a diffusion equation (diffusion coefficient  $D_c$ ), with additional (point) sources. In addition, we also use a sink term to describe a possible decay (e.g., due to bulk reactions) of the solute.

$$\partial_t c(\mathbf{r}, t) = D_c \Delta c - k_d c + k_0 \sum_{i=1}^N \sum_{k=k'} \delta(\mathbf{r} - \mathbf{r}_{i,k}) \quad (2)$$

The system of equations (eqs 1, 2) is numerically solved in two spatial dimensions (2D) with periodic boundary conditions.

**Mean Velocity.** The averaged velocities of the “molecular swimmers” consisting of one to three particles were calculated by averaging over at least 30 independent trajectories with a minimum time of 10 s and a sampling rate of 40/s (see Table 1). The relatively large standard deviation is due to the rather short trajectory length which has been used, in analogy to our experiments, to calculate the mean speed.

## ■ ASSOCIATED CONTENT

### Supporting Information

The Supporting Information is available free of charge at <https://pubs.acs.org/doi/10.1021/acs.langmuir.0c01568>.

Additional characterization, size distribution histogram, zoomed-in SEM image, MSD data, additional assembly trajectories, analytic prediction of swimming velocities, STEM–EDX analysis, and snapshots of positively functionalized swimmers (PDF)

Motion pattern of single ellipsoid particles (0.3% H<sub>2</sub>O<sub>2</sub>, 100% UV illumination) (AVI)

Simulated motion pattern of single ellipsoid particles and assembly (activation after 3 s) (AVI)

Motion of different active assemblies (0.3% H<sub>2</sub>O<sub>2</sub>, 100% UV illumination) (AVI)

Formation and motion of functionalized active assemblies (0.3% H<sub>2</sub>O<sub>2</sub>, 100% green illumination, 100% UV illumination) (AVI)

## AUTHOR INFORMATION

### Corresponding Author

**Juliane Simmchen** – Physical Chemistry, TU Dresden, 01069 Dresden, Germany; [orcid.org/0000-0001-9073-9770](https://orcid.org/0000-0001-9073-9770); Phone: +49 351 463-37433; Email: [juliane.simmchen@tu-dresden.de](mailto:juliane.simmchen@tu-dresden.de)

### Authors

**Sandra Heckel** – Physical Chemistry, TU Dresden, 01069 Dresden, Germany

**Jens Grauer** – Theoretical Physics II: Soft Matter, Heinrich Heine University Düsseldorf, 40225 Düsseldorf, Germany

**Maria Semmler** – Physical Chemistry, TU Dresden, 01069 Dresden, Germany

**Thomas Gemming** – Institute of Complex Materials, Leibniz IFW Dresden, 01069 Dresden, Germany

**Hartmut Löwen** – Theoretical Physics II: Soft Matter, Heinrich Heine University Düsseldorf, 40225 Düsseldorf, Germany

**Benno Liebchen** – Institute of Condensed Matter Physics, TU Darmstadt, 64289, Germany

Complete contact information is available at:

<https://pubs.acs.org/10.1021/acs.langmuir.0c01568>

### Notes

The authors declare no competing financial interest.

## ACKNOWLEDGMENTS

The authors thank Helena Decker for TEM images. This work was supported by a Freigeist fellowship from the Volkswagen foundation (grant number 91619) and by the DFG within the project LO 418/17-2.

## REFERENCES

- (1) Jurado-Sánchez, B.; Pacheco, M.; Rojo, J.; Escarpa, A. Magnetocatalytic Graphene Quantum Dots Janus Micromotors for Bacterial Endotoxin Detection. *Angew. Chem., Int. Ed.* **2017**, *56*, 6957–6961.
- (2) Sonntag, L.; Simmchen, J.; Magdanz, V. Nano- and Micromotors Designed for Cancer Therapy. *Molecules* **2019**, *24*, 3410.
- (3) Wang, L.; Kaeppler, A.; Fischer, D.; Simmchen, J. Photocatalytic TiO<sub>2</sub> Micromotors for Removal of Microplastics and Suspended Matter. *ACS Appl. Mater. Interfaces* **2019**, *11*, 32937–32944.
- (4) Wang, W.; Lv, X.; Moran, J. L.; Duan, S.; Zhou, C. A practical guide to active colloids: choosing synthetic model systems for soft matter physics research. *Soft Matter* **2020**, *16*, 3846.
- (5) Shemi, O.; Solomon, M. J. Self-Propulsion and Active Motion of Janus Ellipsoids. *J. Phys. Chem. B* **2018**, *122*, 10247–10255.
- (6) Yu, T.; Chuphal, P.; Thakur, S.; Reigh, S. Y.; Singh, D. P.; Fischer, P. Chemical micromotors self-assemble and self-propel by

spontaneous symmetry breaking. *Chem. Commun.* **2018**, *54*, 11933–11936.

(7) Wang, Z.; Wang, Z.; Li, J.; Tian, C.; Wang, Y. Active colloidal molecules assembled via selective and directional bonds. *Nat. Commun.* **2020**, *11*, 2670.

(8) Simmchen, J.; Baeza, A.; Ruiz, D.; Esplandiú, M. J.; Vallet-Regí, M. Asymmetric hybrid silica nanomotors for capture and cargo transport: Towards a novel motion-based DNA sensor. *Small* **2012**, *8*, 2053–2059.

(9) Niu, R.; Palberg, T. Modular approach to microswimming. *Soft Matter* **2018**, *14*, 7554–7568.

(10) Ebbens, S.; Jones, R. A.; Ryan, A. J.; Golestanian, R.; Howse, J. R. Self-assembled autonomous runners and tumblers. *Phys. Rev. E: Stat., Nonlinear, Soft Matter Phys.* **2010**, *82*, No. 015304(R).

(11) Nourhani, A.; Brown, D.; Pletzer, N.; Gibbs, J. G. Engineering Contactless Particle-Particle Interactions in Active Microswimmers. *Adv. Mater.* **2017**, *29*, 1703910.

(12) Krüger, C.; Bahr, C.; Herminghaus, S.; Maass, C. C. Dimensionality matters in the collective behaviour of active emulsions. *Eur. Phys. J. E* **2016**, *39*, 64.

(13) Niu, R.; Fischer, A.; Palberg, T.; Speck, T. Dynamics of Binary Active Clusters Driven by Ion-Exchange Particles. *ACS Nano* **2018**, *12*, 10932–10938.

(14) Niu, R.; Botin, D.; Weber, J.; Reinmüller, A.; Palberg, T. Assembly and Speed in Ion-Exchange-Based Modular Phoretic Microswimmers. *Langmuir* **2017**, *33*, 3450–3457.

(15) Liebchen, B.; Niu, R.; Palberg, T.; Löwen, H. Unraveling modular microswimmers: From self-assembly to ion-exchange-driven motors. *Phys. Rev. E* **2018**, *98*, 052610.

(16) Kei Cheang, U.; Meshkati, F.; Kim, H.; Lee, K.; Fu, H. C.; Kim, M. J. Versatile microrobotics using simple modular subunits. *Sci. Rep.* **2016**, *6*, 30472.

(17) Yan, J.; Han, M.; Zhang, J.; Xu, C.; Luijten, E.; Granick, S. Reconfiguring active particles by electrostatic imbalance. *Nat. Mater.* **2016**, *15*, 1095–1099.

(18) Ma, F.; Wang, S.; Wu, D. T.; Wu, N. Electric-field-induced assembly and propulsion of chiral colloidal clusters. *Proc. Natl. Acad. Sci. U.S.A.* **2015**, *112*, 6307–6312.

(19) Schmidt, F.; Liebchen, B.; Löwen, H.; Volpe, G. Light-controlled assembly of active colloidal molecules. *J. Chem. Phys.* **2019**, *150*, 094905.

(20) Mallory, S. A.; Cacciuto, A. Activity-assisted self-assembly of colloidal particles. *Phys. Rev. E* **2016**, *94*, 022607.

(21) Bär, M.; Großmann, R.; Heidenreich, S.; Peruani, F. Self-Propelled Rods: Insights and Perspectives for Active Matter. *Annu. Rev. Condens. Matter Phys.* **2020**, *11*, 441–466.

(22) Löwen, H. Active colloidal molecules. *Europhys. Lett.* **2018**, *121*, S8001.

(23) Martínez-Pedrero, F.; Massana-Cid, H.; Tierno, P. Assembly and Transport of Microscopic Cargos via Reconfigurable Photo-activated Magnetic Microdockers. *Small* **2017**, *13*, 1603449.

(24) Martínez-Pedrero, F.; Navarro-Argemí, E.; Ortiz-Ambriz, A.; Pagonabarraga, I.; Tierno, P. Emergent hydrodynamic bound states between magnetically powered micropellers. *Sci. Adv.* **2018**, *4*, No. eaap9379.

(25) Heckel, S.; Simmchen, J. Photocatalytic BiVO<sub>4</sub> Microswimmers with Bimodal Swimming Strategies. *Adv. Intell. Syst.* **2019**, *1*, 1900093.

(26) Villa, K.; Novotný, F.; Zelenka, J.; Browne, M. P.; Ruml, T.; Pumera, M. Visible-Light-Driven Single-Component BiVO<sub>4</sub> Micro-motors with the Autonomous Ability for Capturing Microorganisms. *ACS Nano* **2019**, *13*, 8135–8145.

(27) Tokunaga, S.; Kato, H.; Kudo, A. Selective preparation of monoclinic and tetragonal BiVO<sub>4</sub> with scheelite structure and their photocatalytic properties. *Chem. Mater.* **2001**, *13*, 4624–4628.

(28) Li, R.; Zhang, F.; Wang, D.; Yang, J.; Li, M.; Zhu, J.; Zhou, X.; Han, H.; Li, C. Spatial separation of photogenerated electrons and holes among {010} and {110} crystal facets of BiVO<sub>4</sub>. *Nat. Commun.* **2013**, *4*, 1432–1437.

- (29) Li, R.; Han, H.; Zhang, F.; Wang, D.; Li, C. Highly efficient photocatalysts constructed by rational assembly of dual-cocatalysts separately on different facets of BiVO<sub>4</sub>. *Energy Environ. Sci.* **2014**, *7*, 1369–1376.
- (30) Lardhi, S.; Cavallo, L.; Harb, M. Significant Impact of Exposed Facets on the BiVO<sub>4</sub> Material Performance for Photocatalytic Water Splitting Reactions. *J. Phys. Chem. Lett.* **2020**, *11*, 5497–5503.
- (31) Perry, R. W.; Holmes-Cerfon, M. C.; Brenner, M. P.; Manoharan, V. N. Two-Dimensional Clusters of Colloidal Spheres: Ground States, Excited States, and Structural Rearrangements. *Phys. Rev. Lett.* **2015**, *114*, 228301.
- (32) van Schooneveld, M. M.; Cormode, D. P.; Koole, R.; Van Wijngaarden, J. T.; Calcagno, C.; Skajaa, T.; Hilhorst, J.; 't Hart, D. C.; Fayad, Z. A.; Mulder, W. J. M.; Meijerink, A. A fluorescent, paramagnetic and PEGylated gold/silica nanoparticle for MRI, CT and fluorescence imaging. *Contrast Media Mol. Imaging* **2010**, *5*, 231–236.
- (33) Liong, M.; Angelos, S.; Choi, E.; Patel, K.; Stoddart, J. F.; Zink, J. I. Mesostructured multifunctional nanoparticles for imaging and drug delivery. *J. Mater. Chem.* **2009**, *19*, 6251–6257.
- (34) Sun, J.; Zhang, H.; Tian, R.; Ma, D.; Bao, X.; Su, D. S.; Zou, H. Ultrafast enzyme immobilization over large-pore nanoscale mesoporous silica particles. *Chem. Commun.* **2006**, *1*, 1322–1324.
- (35) Palacci, J.; Sacanna, S.; Steinberg, A. P.; Pine, D. J.; Chaikin, P. M. Living crystals of light-activated colloidal surfers. *Science* **2013**, *339*, 936–940.
- (36) Jiang, H.; Dai, H.; Meng, X.; Ji, K.; Zhang, L.; Deng, J. Porous olive-like BiVO<sub>4</sub>: Alchohydrothermal preparation and excellent visible-light-driven photocatalytic performance for the degradation of phenol. *Appl. Catal., B* **2011**, *105*, 326–334.
- (37) Tinevez, J.-Y.; Perry, N.; Schindelin, J.; Hoopes, G. M.; Reynolds, G. D.; Laplantine, E.; Bednarek, S. Y.; Shorte, S. L.; Eliceiri, K. W. TrackMate: An open and extensible platform for single-particle tracking. *Methods* **2017**, *115*, 80–90.
- (38) Tarantino, N.; Tinevez, J.-Y.; Crowell, E. F.; Boisson, B.; Henriques, R.; Mhlanga, M.; Agou, F.; Israël, A.; Laplantine, E. Tnf and il-1 exhibit distinct ubiquitin requirements for inducing NEMO-IKK supramolecular structures. *J. Cell Biol.* **2014**, *204*, 231–245.
- (39) Hauke, F.; Löwen, H.; Liebchen, B. Clustering-induced velocity-reversals of active colloids mixed with passive particles. *J. Chem. Phys.* **2020**, *152*, 014903.
- (40) Saha, S.; Golestanian, R.; Ramaswamy, S. Clusters, asters, and collective oscillations in chemotactic colloids. *Phys. Rev. E: Stat., Nonlinear, Soft Matter Phys.* **2014**, *89*, 062316.
- (41) Pohl, O.; Stark, H. Dynamic clustering and chemotactic collapse of self-phoretic active particles. *Phys. Rev. Lett.* **2014**, *112*, 238303.
- (42) Scagliarini, A.; Pagonabarraga, I. Non-equilibrium phases in suspensions of self-propelled colloidal particles controlled by phoretic mobility and hydrodynamics. *arXiv* **2016**, *2*, 1–8.
- (43) Liebchen, B.; Marenduzzo, D.; Pagonabarraga, I.; Cates, M. E. Clustering and Pattern Formation in Chemorepulsive Active Colloids. *Phys. Rev. Lett.* **2015**, *115*, 258301.
- (44) Baskaran, A.; Cristina Marchetti, M. Hydrodynamics of self-propelled hard rods. *Phys. Rev. E: Stat., Nonlinear, Soft Matter Phys.* **2008**, *77*, 011920.
- (45) Janssen, L. M. C.; Kaiser, A.; Löwen, H. Aging and rejuvenation of active matter under topological constraints. *Sci. Rep.* **2017**, *7*, 5667.
- (46) Perrin, F. Mouvement brownien d'un ellipsoïde—I. Dispersion diélectrique pour des molécules ellipsoïdales. *J. Phys. Radium* **1934**, *5*, 497–511.